

# Towards Generalized Proactive Defense against Face Swapping with Contour-Hybrid Watermark

Ruiyang Xia · Dawei Zhou · Decheng Liu · Lin Yuan · Jie Li · Nannan Wang · Xinbo Gao

Received: date / Accepted: date

**Abstract** Face swapping, recognized as a privacy and security concern, has prompted considerable defensive research. With the advancements in AI-generated content, the discrepancies between the real and swapped faces have become nuanced. Considering the difficulty of forged traces detection, we shift the focus to the face swapping purpose and proactively embed elaborate watermarks against unknown face swapping techniques. Given that the constant purpose is to swap the original face identity while preserving the background, we concentrate on the regions surrounding the face to

ensure robust watermark generation, while embedding the contour texture and face identity information to achieve progressive image determination. The watermark is located in the facial contour and contains hybrid messages, dubbed the **contour-hybrid watermark** (CMark). Our approach generalizes face swapping detection without requiring any swapping techniques during training and the storage of large-scale messages in advance. Experiments conducted across 8 face swapping techniques demonstrate the superiority of our approach compared with state-of-the-art passive and proactive detectors while achieving a favorable balance between the image quality and watermark robustness.

**Keywords** Face Swapping · Deepfake Detection · Proactive Defense · Information Hiding

## 1 Introduction

With the development of AI-generated content (AIGC) towards high fidelity and low complexity Wu et al (2023a), it is convenient to generate fictitious but vivid media. However, this convenience raises the forgery dissemination, especially for face swapping techniques. Recent reports reveal a 704% surge in the use of face swapping techniques in 2023 to bypass identity verification, underscoring face swapping as the most prevalent deepfake iProov (2024). To make AI trustworthy Kaur et al (2022); Li et al (2023), face swapping detection is naturally introduced Wang et al (2024b).

Previous passive detectors mainly focus on the pixel discrepancies between the real and swapped images Huang et al (2023a); Dong et al (2023); Xia et al (2024); Liu et al (2025a); Cheng et al (2024); Tao et al (2025); Liu et al (2025b). However, their detection performance

Ruiyang Xia  
Xidian University, Xi'an 710071, Shaanxi, China  
E-mail: [ryon@stu.xidian.edu.cn](mailto:ryon@stu.xidian.edu.cn)

Dawei Zhou  
City University of Macau, Macao Special Administrative Region, China  
E-mail: [dwzhou.xidian@gmail.com](mailto:dwzhou.xidian@gmail.com)

Decheng Liu  
Xidian University, Xi'an 710071, Shaanxi, China  
E-mail: [dchliu@xidian.edu.cn](mailto:dchliu@xidian.edu.cn)

Lin Yuan  
Chongqing University of Posts and Telecommunications, Chongqing 400065, China  
E-mail: [yuanlin@cqupt.edu.cn](mailto:yuanlin@cqupt.edu.cn)

Jie Li  
Xidian University, Xi'an 710071, Shaanxi, China  
E-mail: [leejie@mail.xidian.edu.cn](mailto:leejie@mail.xidian.edu.cn)

Nannan Wang  
Xidian University, Xi'an 710071, Shaanxi, China  
E-mail: [nnwang@xidian.edu.cn](mailto:nnwang@xidian.edu.cn)

Xinbo Gao  
Xidian University, Xi'an 710071, Shaanxi, China  
E-mail: [xbgao@mail.xidian.edu.cn](mailto:xbgao@mail.xidian.edu.cn)

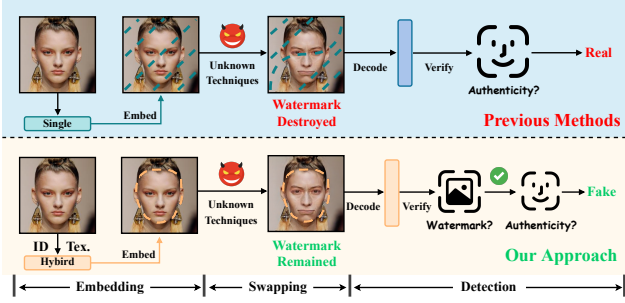


Fig. 1: **Comparison of proactive detection.** Previous methods embed a watermark with a single-type message into the entire image. However, we embed the watermark into the facial contour to ensure robustness, while integrating identity and contour texture (Tex.) into the message to achieve progressive determination.

is constrained by diverse forged traces and continuously decreased discrepancies Walczyna and Piotrowski (2023). Proactive paradigms, which embed watermarks in images and trace them after forgery, have been proposed to improve detection accuracy and make determined evidence more intuitive Wang et al (2023); Wu et al (2023b); Zhao et al (2023b); Wang et al (2024a).

Conventionally, as shown in Fig. 1, a single-type message, such as random Gaussian variables Wang et al (2021); Neekhara et al (2022); Wu et al (2023b), is allocated to each image. The watermark is then generated and applied across the entire image. Although the robustness of the watermark remains when training with specific face swapping techniques Neekhara et al (2022); Wu et al (2023b); Wang et al (2023, 2024a), according to the reported bit error rates from Wang et al (2024a), some proactive detectors become sensitive when exposed to unknown techniques, thereby resulting in poor generalization. Furthermore, this type of message only ensures the determination of the images that have already been incorporated into the watermarks. However, the distinction between the watermarked and non-watermarked images is ignored, which limits the applicability of the proactive detection methods in the real-world as there are many non-watermarked images spread on the websites. Therefore, a generalized and applicable proactive approach is needed imminently.

Starting from the constant face swapping purpose, *i.e.*, **swapping the original face identity while preserving the background**. A novel proactive detection approach dubbed **contour-hybrid watermark (CMark)** is proposed to effectively defend against unknown face swapping techniques. Unlike previous works that embed a single-type message into an entire image Zhu et al (2018); Fang et al (2022); Huang et al (2023b); Wu et al (2023b), the watermark location and

message are carefully designed in Fig. 1 for robust watermark generation and progressive image determination. As to the location, we focus on the contour region, which reduces the interferences brought by face swapping and malicious background cropping during watermark decoding. Moreover, the local watermark facilitates the visual quality as most regions of the watermarked images are consistent with the originals. Given that the similar contour but different identity for real and swapped images, we integrate the contour texture and face identity information as the messages. Consequently, the verification is separated into two steps. The message involving contour texture is initially verified to determine whether the image is watermarked, while the decoded identity message is subsequently verified for authenticity determination. Different from relevant methods Wang et al (2023); Neekhara et al (2022); Zhao et al (2023b); Zhang et al (2024b), our approach is self-verifiable Wang et al (2024a), which verifies the decoded messages without requiring the corresponding preset messages, thereby efficiently saving the message storage. Before verification, messages are encrypted to ensure the security of the proposed proactive detector.

The main contributions can hence be summarized as:

- To make the proactive defense approach generalizes to unknown face swapping techniques, CMark is proposed based on the constant swapping purpose. To the best of our knowledge, we are the early exploration that simultaneously concentrates on designing the watermark location and message, which ensures the visual quality, watermark robustness, and progressive image determination.
- Our approach achieves accurate detection without requiring any face swapping techniques during the model training. Furthermore, the self-verifiable property is maintained to save the storage of messages *w.r.t.* all watermarked images.
- Extensive experiments across 8 prevalent face swapping techniques demonstrate the superiority of our approach compared with passive and proactive detectors. Moreover, the results regarding visual quality and watermark robustness underscore the favorable balance achieved by the CMark model.

The rest of this paper is organized as follows. Sect. 2 briefly reviews the related work. Sect. 3 lists the motivation and threat model as the prerequisite of the proposed approach. Sect. 4 thus presents the detail of the proposed CMark framework. Sect. 5 shows the experimental results and corresponding analysis. The limitations and future perspective are presented in Sect. 6. Finally, the conclusion is summarized in Sect. 7.

## 2 Related Work

### 2.1 Face Swapping Techniques

Early research swap faces with manual techniques. Given a source and target image, The work in [Wu et al \(2020\)](#) decomposed the facial areas of the source and target images into Delaunay triangles. The source face is swapped by replacing its triangles with the corresponding wrapped ones from the target face. However, in cases with substantial discrepancies in facial attributes between the source and target faces, the results suffered from reduced fidelity. Deep learning is then introduced to elevate the fidelity of the generated swapped images. Specifically, reconstruction-based methods [Xu et al \(2022\)](#); [Li et al \(2019\)](#); [Chen et al \(2020\)](#) mainly focus on extracting source attributes and target identity through reconstruction learning before integration. Due to entanglement of features in attributes and identity, StyleGAN-based methods [Zhu et al \(2021\)](#); [Liu et al \(2023\)](#) are proposed to disentangle face images into multiple representative latent vectors [Karras et al \(2019\)](#), thereby achieving more fidelity face images with detailed texture preservation. Based on the powerful diffusion models [Song et al \(2020\)](#); [Ho et al \(2020\)](#); [Nichol and Dhariwal \(2021\)](#); [Rombach et al \(2021\)](#) that stabilize the training process and progressively fit the complex distribution, diffusion-based methods [Kim et al \(2022\)](#); [Zhao et al \(2023a\)](#) have emerged to elevate the fidelity across varying scales.

While various swapping techniques produce distinct forged traces, their overarching purpose remains consistent. This fundamental principle enables the establishment of a generalized face swapping detection model.

### 2.2 Face Forgery Detection

Prevalent face forgery detection can be categorized as model-based and data-based methods [Wang et al \(2024b\)](#). The former aims to improve the detection model awareness of forged traces within the swapped images. For instance, IID [Huang et al \(2023a\)](#) decomposed the swapped image into explicit and implicit embedding for detection. F3Net [Qian et al \(2020\)](#) simultaneously analyzed the face images from the spatial and frequency domain. RECCE [Cao et al \(2022\)](#) amplified the discrepancies between the real and swapped images through face reconstruction. To decrease the overfitting of the evident traces from the specific forgery techniques, data-based methods [Li et al \(2020\)](#); [Shiohara and Yamasaki \(2022\)](#); [Xia et al \(2024\)](#); [Zhou et al \(2024\)](#); [Yan et al \(2024\)](#) try to emphasize the common forged traces by simulating the color mismatching, face

blurring, and blending inconsistency into the real images. For example, [Li et al \(2020\)](#) simulate the face swapping process by deliberately incorporating inconsistency within the face edge. Considering the complexity of similar face searching between the source and target face, [Shiohara and Yamasaki \(2022\)](#) proposed a self-blending strategy and simulated more forged traces. Subsequently, [Xia et al \(2024\)](#) strengthened the local hard forgery traces for training through the interaction with the detector perception. [Zhou et al \(2024\)](#) and [Yan et al \(2024\)](#) further expanded the self-blending strategy to the frequency and temporal domain, respectively.

Nevertheless, the forged traces generated from the swapped techniques are becoming imperceptible. Previous passive detectors may prove ineffective against recent advancements such as StyleGAN-based or diffusion-based methods. Proactive paradigms are thus introduced to embed watermarks and analyze the change of the watermark after forgery, which have been proposed to improve detection accuracy.

### 2.3 Deep Image Watermarking

Beyond visible watermarks, the pursuit of invisibility and robustness has become a primary focus in related [Zhu et al \(2018\)](#); [Jia et al \(2021\)](#); [Huang et al \(2023b\)](#); [Fang et al \(2022\)](#). [Zhu et al \(2018\)](#) first proposed an end-to-end robust watermark network, which comprises an image encoder, a random noise layer, and a watermark decoder. Considering that JPEG is non-differential to the network, MBRS [Jia et al \(2021\)](#) randomly attached each sample within a batch with identical mapping, simulated JPEG, or real JPEG compression. PIMOG [Fang et al \(2022\)](#) formulated the most influenced distortions occurring during the screen-capturing process within the noise pool. ARWGAN [Huang et al \(2023b\)](#) integrated dense blocks and attention mechanism to enhance the image quality and watermark robustness. As the generated watermarked images are employed for copyright tracing, recent detection methods have increasingly focused on proactively embedding watermarks into images to monitor the variations of watermark [Zhao et al \(2023b\)](#); [Neekhara et al \(2022\)](#); [Wu et al \(2023b\)](#); [Wang et al \(2024a, 2023\)](#). Facesigns [Neekhara et al \(2022\)](#) proposed a semi-fragile model to make the generated watermark sensitive to the forgery techniques. SepMark [Wu et al \(2023b\)](#) developed robust and semi-fragile branches to assess their decoding consistency. IDMark [Zhao et al \(2023b\)](#) introduced watermarked identity features and further correlated the features with preset watermarks to determine image authenticity. The work in [Wang et al \(2023\)](#) compared the watermark with the stored protected identity

messages. Wang et al (2024a) achieves self-verifiable by generating landmark watermark can compare it with the landmark from the forged images.

Due to the diversity of face swapping techniques, the presence of non-watermarked images, and the large volume of watermarked images, it poses significant challenges for existing methods in real-world applications.

### 3 Motivation and Threat Model

#### 3.1 Motivation

**Diverse forged traces but constant purpose.** The swapped face images under different techniques are illustrated in Fig. 2(a), highlighting that the forged traces are inherently dependent on specific techniques. For example, FaceSwap Wu et al (2020) brings color mismatching, MobileFS Xu et al (2022) and FaceShifter Li et al (2019) emerge artifacts within the face. Furthermore, the decreased NIQE Mittal et al (2012) and FID Heusel et al (2017) scores indicate the continuously improved quality of the swapped images, which further increases the detection difficulties. While numerous techniques are unknown to defenders, they share a common purpose: swapping the original identity while preserving the background. Furthermore, since face swapping mainly modifies the internal attributes, the qualitative result in Fig. 2(b) shows minimal deviations in contour landmarks between the real and swapped face. Quantitative analysis reveals that most landmark discrepancies between the paired images have less than 5 average L1 distance. These observations motivate a face-aware watermarking strategy, wherein the watermark distribution is controlled to ensure robustness and face swapping detection is achieved through message tailoring.

**Omission in previous proactive detectors.** Four problems that are necessary but less discussed in previous proactive methods: (1) Although the authenticity of watermarked images can be assessed, the determination between the watermarked and non-watermarked images is frequently neglected. (2) Proactive detection is typically achieved through training with the corresponding forgery techniques, which hinders the generalized detection due to the varying nature of forgery traces. (3) Certain proactive methods depend on matching preset messages stored in the memory, which imposes considerable strain on storage resources. (4) The robustness of the watermark remains inadequately addressed when face swapping techniques are combined with image distortions. As proactive detection continues to evolve, more considerations are essential to improve the practicality of the proactive detectors in real-world scenarios.

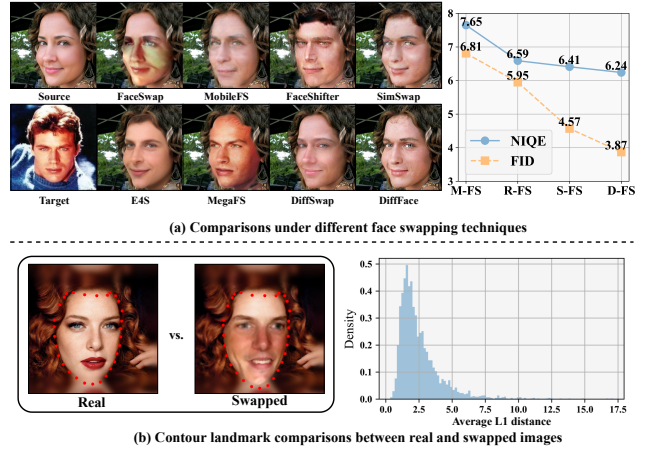


Fig. 2: (a) Qualitative and quantitative face swapping comparisons. ‘M-FS’, ‘R-FS’, ‘S-FS’, and ‘D-FS’ denote manual method (FaceSwap), reconstruction-based methods (MobileFS, Faceshifter, and SimSwap), StyleGAN-based methods (E4S and MegaFS), and Diffusion-based methods (DiffSwap and DiffFace). FID is computed by averaging the features from different layers of Szegedy et al (2016). (b) Qualitative and quantitative contour landmark comparisons under FaceSwap Wu et al (2020) on  $256 \times 256$  resolution.

#### 3.2 Multiple Threatening Cases

Given that the variety of situations in real-world scenarios, we outline three representative threatening cases based on a security assumption as follows:

- **Security assumption:** All models are deployed **securely** on clients, while message verification is conducted on a central platform, ensuring that the model parameters and the verified process are **forbidden** for attackers. Accessible things for them are images posted on websites and messages intercepted during client-platform communication.
- **Case 1:** Before swapping the watermarked face images, attackers extract the corresponding backgrounds and intentionally crop some regions to erase the embedded watermarks.
- **Case 2:** After swapping the watermarked face images, attackers impose different images distortions to interfere with the watermark decoding process.
- **Case 3:** During the communication between clients and the platform, attackers surveil network traffic to intercept the unencrypted decoded messages. Subsequently, they infiltrate the communication channel and introduce tampered messages into the verification process, thereby hindering the confidence.



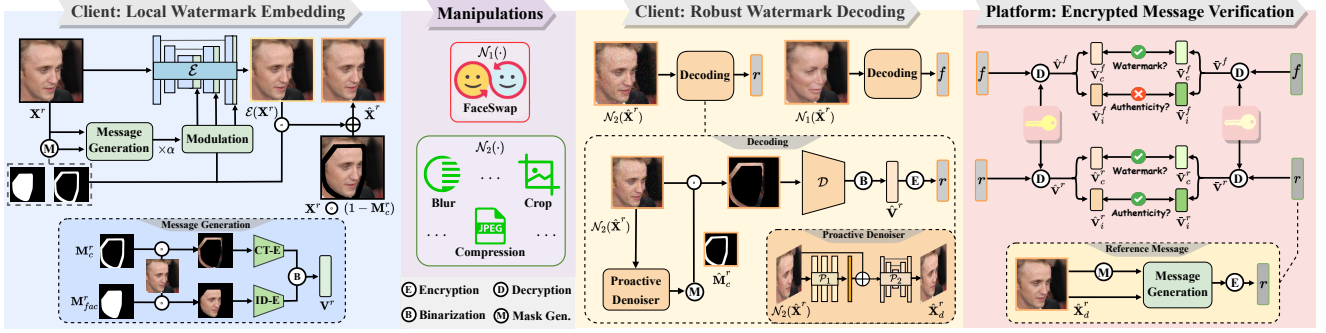


Fig. 3: **Pipeline of our proposed CMark model.** Firstly, the client generates message  $\mathbf{V}^r$  by integrating features from the contour texture extractor (CT-E) and face identity extractor (ID-E). The message is then embedded into the facial contour through watermark encoder  $\mathcal{E}$  after scaling by a strength factor  $\alpha$ . **Secondly**, for the watermarked image  $\hat{\mathbf{X}}^r$  subjected to random manipulations, the robust watermark is decoded by inputting the contour region of the manipulated  $\hat{\mathbf{X}}^r$  into the watermark decoder  $\mathcal{D}$ . **Finally**, after sending the encrypted messages to the platform for decryption, the decoded message  $\hat{\mathbf{V}}$  is verified against the reference message  $\bar{\mathbf{V}}$  to determine the watermark existence and the image authenticity. ‘Gen.’ denotes ‘Generation’.

## 4 Contour-Hybrid Watermark

### 4.1 Problem Formulation

Given a real image  $\mathbf{X}^r \in \mathbb{R}^{H \times W \times 3}$  with identity message  $\mathbf{V}_i^r \in \{0, 1\}^{1 \times C}$ , the image is decomposed into a face  $\mathbf{R}_{fac}^r$  and background region  $\mathbf{R}_{bac}^r \in \mathbb{R}^{H \times W \times 3}$ . Assuming that unknown face swapping techniques are employed to tamper the  $\mathbf{X}^r$  as  $\mathbf{X}^f$ , both images meet  $\mathbf{R}_{bac}^r \sim \mathbf{R}_{bac}^f$ ,  $\mathbf{R}_{fac}^r \sim \mathbf{R}_{fac}^f$ , and  $\mathbf{V}_i^r \neq \mathbf{V}_i^f$ . Therefore, three stages are involved in the model to proactively defend against such techniques. As shown in Fig. 3, after extracting the contour mask  $\mathbf{M}_c^r \in \{0, 1\}^{H \times W \times 3}$ , a watermark is imperceptibly embedded within contour region  $\mathbf{R}_c^r$  via an encoder  $\mathcal{E}$ . When the watermarked image  $\hat{\mathbf{X}}^r \in \mathbb{R}^{H \times W \times 3}$  is manipulated (either face swapping  $\mathcal{N}_1(\cdot)$  or normal distortions  $\mathcal{N}_2(\cdot)$ ), the robust watermark is decoded by  $\mathcal{D}$  and transmitted to the platform for verification. The decoded message comprises the contour texture  $\hat{\mathbf{V}}_c$  and face identity message  $\hat{\mathbf{V}}_i$ , which are verified with the reference messages  $\mathbf{V}_c$  and  $\bar{\mathbf{V}}_i$  from the denoised image  $\hat{\mathbf{X}}_d$  to enable progressive determination. Based on the security assumption, the decoded and reference messages are encrypted before verification.

### 4.2 Local Watermark Embedding

**Watermark location.** Due to the severe tampering within the  $\mathbf{R}_{fac}$  after face swapping, avoiding the area during embedding is helpful to preserve the generated watermark. Considering the threatening Case 1, embedding the watermark across the entire  $\mathbf{R}_{bac}$  also introduces vulnerabilities especially when attackers immensely crop the background. Given that malicious

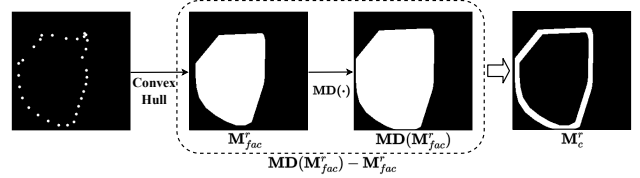


Fig. 4: **Illustration of the facial contour mask generation.**  $\text{MD}(\cdot)$  denotes the morphological dilation function. This process confines the watermark to sub-regions of the background, rendering it unaffected by internal facial manipulations.

cropping should not affect the facial attributes within the image, the contour region surrounds the face and encompasses peripheral attributes such as ears and hair (see Fig. 3), which is a beneficial region to embed a watermark resilient to such intentional distortions. Based on the landmark similarity of face contours between the real and swapped images in Fig. 2(b), focusing on the region also offers a feasible solution for constructing watermarks robust to face swapping. Furthermore, localized embedding within the contour ensures visual quality and semantic consistency, as the majority of regions in watermarked images are consistent with the originals. To make the watermark localize the contour region, upon detecting the facial landmarks of  $\mathbf{X}^r$ , a facial mask  $\mathbf{M}_{fac}^r$  is generated in Fig. 4. Based on the morphological dilation function  $\text{MD}(\cdot)$ , the contour mask  $\mathbf{M}_c^r$  is derived as  $\text{MD}(\mathbf{M}_{fac}^r) - \mathbf{M}_{fac}^r$ , which belongs to the sub-regions of the background and serves as the constraint for watermark embedding. Since some landmark discrepancies between real and swapped images lead to contour mark inconsistency, the iteration of the

morphological dilation is randomized during the training stage to simulate the contour mask diversity.

**Watermark message.** The determination between real and fake images from previous proactive methods is based on the matching degree between the preset and decoded messages. As non-watermarked images naturally own the mismatching property, it is unreasonable to classify non-watermarked images posted on websites as watermarked fakes. The contour textures—being similar in both real and swapped images—can be selected as one type of message to effectively filter out non-watermarked images. Moreover, considering the identity discrepancy between the real and swapped images, face swapping detection is achieved by comparing the messages involved in identity information. Consequently, the extracted  $\mathbf{R}_c^r$  and  $\mathbf{R}_{fac}^r$  are used to generate contour and identity features through the pretrained models Zhang et al (2018); Deng et al (2019). Given that the features are represented in high dimensions, embedding them fully into the image proves challenging and brings irrelevant noises. Global average pooling (GAP) and principal component analysis (PCA) Abdi and Williams (2010) are thus applied to squeeze the spatial and channel dimensions of the extracted features, respectively. To account for inconsistent magnitudes among input images, the squeezed features are scaled to  $[-1, 1]$ . Each element of the scaled identity  $\mathbf{F}_i^r$  and contour features  $\mathbf{F}_c^r \in \mathbb{R}^{1 \times C}$  is binarized into  $\mathbf{V}_i^r$  and  $\mathbf{V}_c^r$  using a threshold of 0. The hybrid message  $\mathbf{V}^r$  is allocated by concatenating  $\mathbf{V}_c^r$  and  $\mathbf{V}_i^r$  as  $\mathbf{V}^r = [\mathbf{V}_c^r; \mathbf{V}_i^r]$ . To ensure imperceptible embedding, the magnitude of  $\mathbf{V}^r$  is regulated by a factor  $\alpha$  as  $\mathbf{V}_\alpha^r \in \{-\alpha, \alpha\}^{1 \times 2C}$ .

**Embedding process.** The process is performed by integrating the  $\mathbf{V}_\alpha^r$  into the original real image. The watermark encoder  $\mathcal{E}$  utilizes an alike UNet architecture to generate encoded images. As to the message  $\mathbf{V}_\alpha^r$ , a combination of multilayer perceptron (MLP) with convolution layers is employed to modulate  $\mathbf{V}_\alpha^r$  at different scales, facilitating the integration of the corresponding image features. To ensure the watermark is localized within the  $\mathbf{R}_c^r$ , the integration at the  $k$ -th layer is constrained by  $\mathbf{M}_c^r$  as follows:

$$\mathbf{h}_k' = \text{SE}([\text{Conv}_{3 \times 3}(\text{MLP}(\mathbf{V}_\alpha^r)) \odot \text{Rz}(\mathbf{M}_c^r); \mathbf{h}_k]), \quad (1)$$

where  $\text{SE}(\cdot)$  represents the squeeze-excitation module Hu et al (2018).  $\text{Rz}(\cdot)$  is the resize function.  $\mathbf{h}_k$  and  $\mathbf{h}_k'$  indicate the original and integrated features at the  $k$ -th layer. After integrating the  $\mathbf{V}_\alpha^r$  into  $\mathbf{X}^r$ , the optimization to the  $\mathcal{E}$  involves the discrepancies between  $\mathbf{X}^r$  and  $\mathcal{E}(\mathbf{X}^r)$ , which is expressed as follows:

$$\mathcal{L}_e = l_{\text{MSE}}(\mathbf{X}^r, \mathcal{E}(\mathbf{X}^r)) + \lambda_1 l_{\text{Adv}}(\mathbf{X}^r, \mathcal{E}(\mathbf{X}^r)), \quad (2)$$

where  $\lambda_1$  is hyperparameter. MSE denotes mean square error.  $l_{\text{Adv}}$  indicates the adversarial loss as follows:

$$l_{\text{Adv}}(\mathbf{X}^r, \mathcal{E}(\mathbf{X}^r)) = -\log(\text{Dis}(\mathbf{X}^r)) - \log(1 - \text{Dis}(\mathcal{E}(\mathbf{X}^r))), \quad (3)$$

where  $\text{Dis}$  is the discriminator from Karras et al (2017). After watermark embedding, the watermarked image  $\hat{\mathbf{X}}^r$  is obtained by following:

$$\hat{\mathbf{X}}^r = \mathbf{X}^r \odot (1 - \mathbf{M}_c^r) + \mathcal{E}(\mathbf{X}^r) \odot \mathbf{M}_c^r. \quad (4)$$

Based on Eq. 4, the watermark involves the designated contour region, which not only ensures the availability of the watermark but also further decreases the visual discrepancy with the original images.

#### 4.3 Robust Watermark Decoding

**Training stage.** Considering the threatening Case 2, various normal distortions  $\mathcal{N}_2(\cdot)$  are introduced to ensure the robust watermark embedded in the  $\mathbf{R}_c^r$ . With a large batch size, each iteration will traverse most of the introduced distortions during training, thereby enabling a comprehensive enhancement in watermark resilience. Face swapping techniques are excluded to mitigate the CMark model overfitting to any specific techniques. The categories of normal distortions are described in the implementation details.

The  $\mathbf{M}_c^r$  is utilized to isolate irrelevant image regions, thereby preventing interference during decoding. Since the decoding process also requires image analysis, the decoder shares a similar structure with the  $\mathcal{E}$  except the message integration. Additionally, to distinguish the non-watermarked images, the optimization of the decoder  $\mathcal{D}$  is formulated as follows:

$$\mathcal{L}_d = \|\mathcal{D}(\mathbf{X}^r \odot \mathbf{M}_c^r)\|_2^2 + \lambda_2 l_{\text{MSE}}(\mathbf{V}_\alpha^r, \mathcal{D}(\mathcal{N}_2(\hat{\mathbf{X}}^r) \odot \mathbf{M}_c^r)), \quad (5)$$

where  $\lambda_2$  is the hyperparameter. The first term represents the decoder output for the non-watermarked real image  $\mathbf{X}^r$ , which is regularized to zero to distinguish the message allocated to the corresponding watermarked image as each element of the message towards 1 or -1. To make the watermark imperceptible and robust, the  $\mathcal{E}$  and  $\mathcal{D}$  are trained end-to-end via  $\mathcal{L}_e + \mathcal{L}_d$ .

In practical decoding process, the contour mask employed comes from the manipulated  $\hat{\mathbf{X}}^r$ . The normal distortions cause the contour mask extracted from the noised images deviates from the clean counterparts, thereby impacting the decoding correctness. To decrease the mask biases, a proactive denoiser  $\mathcal{P}$  is introduced to restore normal distorted images. The initial module  $\mathcal{P}_1$  in Fig. 5 estimates randomly distributed

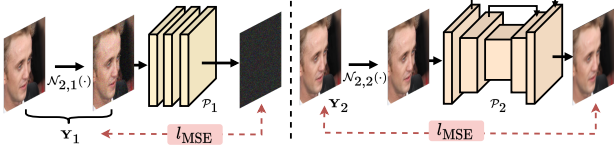


Fig. 5: Illustration of the proposed denoiser modules,  $\mathcal{P}_1$  and  $\mathcal{P}_2$ , during the training phase.

noise, such as Gaussian Noise, while  $\mathcal{P}_2$  recovers details lost due to blurring or compression. The supervision  $\mathbf{Y}_1 \in \mathbb{R}^{H \times W \times 3}$  corresponds to the residual mapping  $\mathbf{X}^r - \mathcal{N}_{2,1}(\mathbf{X}^r)$ , where  $\mathcal{N}_{2,1}(\cdot)$  denotes random noise. The supervision  $\mathbf{Y}_2$  equals  $\mathbf{X}^r$  for denoiser module  $\mathcal{P}_2$  and  $\mathcal{N}_{2,2}(\cdot)$  involves blur or compression. The optimization of the  $\mathcal{P}$  is expressed as follows:

$$\mathcal{L}_p = l_{\text{MSE}}(\mathbf{Y}_1, \mathcal{P}_1(\mathcal{N}_{2,1}(\mathbf{X}^r))) + l_{\text{MSE}}(\mathbf{Y}_2, \mathcal{P}_2(\mathcal{N}_{2,2}(\mathbf{X}^r))). \quad (6)$$

**Testing stage.** After generating the watermarked image  $\hat{\mathbf{X}}^r$ , the denoised image  $\hat{\mathbf{X}}_d$  is computed by:

$$\hat{\mathbf{X}}_d = \mathcal{P}_2(\mathcal{P}_1(\mathcal{N}(\hat{\mathbf{X}}^r)) + \mathcal{N}(\hat{\mathbf{X}}^r)), \quad (7)$$

where  $\mathcal{N}(\cdot)$  encompasses face swapping  $\mathcal{N}_1(\cdot)$  and normal distortions  $\mathcal{N}_2(\cdot)$ . Based on the image  $\mathcal{N}(\hat{\mathbf{X}}^r)$  and the extracted mask  $\hat{\mathbf{M}}_c$  from the denoised image  $\hat{\mathbf{X}}_d$ , the decoded message  $\hat{\mathbf{V}} \in \{-1, 1\}^{1 \times 2C}$  is obtained by binarizing the result  $\mathcal{D}(\mathcal{N}(\hat{\mathbf{X}}^r) \odot \hat{\mathbf{M}}_c)$ .

#### 4.4 Encrypted Message Verification

To achieve self-verification and thus avoid the storage of massive preset messages, we verify the decoded message  $\hat{\mathbf{V}}$  with the reference counterpart  $\bar{\mathbf{V}} \in \{-1, 1\}^{1 \times 2C}$ . Since the normal distortions interfere with verification,  $\bar{\mathbf{V}}$  comes from the denoised image  $\hat{\mathbf{X}}_d$  and is extracted based on the same pretrained models [Deng et al \(2019\)](#); [Zhang et al \(2018\)](#). Considering the threatening Case 3, these messages should be encrypted to safely transmit to the platform for verification. To prevent the leakage of both the  $\hat{\mathbf{V}}$  and  $\bar{\mathbf{V}}$  during communication, two distinct public keys are employed for encryption. This scheme ensures that attackers can not deduce the determined result upon intercepting these encrypted messages, as the encrypted  $\hat{\mathbf{V}}$  and  $\bar{\mathbf{V}}$  remain different regardless of whether their messages are consistent.

Given the potential for key exposure on the client sides, we adopt an asymmetric strategy by assigning public keys to the clients for encryption and corresponding private keys to the platform for decryption. Based on the Rivest-Shamir-Adleman (RSA) algorithm [Rivest](#)

#### Algorithm 1 Encrypted Message Verification

---

**Input:**  $\mathbf{E}_{\hat{\mathbf{v}}}$ : Encrypted decoded message;  $\mathbf{E}_{\bar{\mathbf{v}}}$ : Encrypted reference message;  $t_1, t_2$ : Detection thresholds;  $d_1, d_2$ : Private keys;  $p_1, p_2, q_1, q_2$ : Prime numbers

**Output:**  $O$ : Predicted output of the manipulated image

- 1:  $O \leftarrow \text{None}$
- 2:  $\hat{\mathbf{V}} = \text{RSA\_De}(\mathbf{E}_{\hat{\mathbf{v}}}, q_1, p_1, d_1), \bar{\mathbf{V}} = \text{RSA\_De}(\mathbf{E}_{\bar{\mathbf{v}}}, q_2, p_2, d_2)$
- 3:  $\hat{\mathbf{V}}_i \leftarrow \hat{\mathbf{V}}[:, 0 : C - 1], \hat{\mathbf{V}}_c \leftarrow \hat{\mathbf{V}}[:, C : 2C - 1]$
- 4:  $\bar{\mathbf{V}}_i \leftarrow \bar{\mathbf{V}}[:, 0 : C - 1], \bar{\mathbf{V}}_c \leftarrow \bar{\mathbf{V}}[:, C : 2C - 1]$
- 5: **if**  $\text{BER}(\hat{\mathbf{V}}_c, \bar{\mathbf{V}}_c) \leq t_1$  **then** // Watermark Judgment
- 6:     **if**  $\text{BER}(\hat{\mathbf{V}}_i, \bar{\mathbf{V}}_i) \leq t_2$  **then** // Authenticity Judgment
- 7:          $O \leftarrow \text{Real}$
- 8:     **else**
- 9:          $O \leftarrow \text{Fake}$
- 10:    **end if**
- 11: **end if**
- 12: **return**  $O$

---

(1978), the message encryption, decryption, and key generation are defined as  $\text{RSA\_En}(\cdot)$ ,  $\text{RSA\_De}(\cdot)$ , and  $\text{RSA\_KeyGen}(\cdot)$ . Let  $\phi = (p-1) \cdot (q-1)$ , where  $p$  and  $q$  are different prime numbers, a pair of public key  $e$  and private key  $d$  are generated by  $\text{RSA\_KeyGen}(\phi)$ . The  $\mathcal{D}$  is assigned a key  $e_1$ , while the face identity and contour texture extractors share another key  $e_2$ . The encrypted messages  $\mathbf{E}_{\hat{\mathbf{v}}}$  and  $\mathbf{E}_{\bar{\mathbf{v}}}$  w.r.t.  $\hat{\mathbf{V}}$  and  $\bar{\mathbf{V}}$  are generated as:

$$\mathbf{E}_{\hat{\mathbf{v}}} = \text{RSA\_En}(\hat{\mathbf{V}}, q_1, p_1, e_1); \mathbf{E}_{\bar{\mathbf{v}}} = \text{RSA\_En}(\bar{\mathbf{V}}, q_2, p_2, e_2). \quad (8)$$

The image can be progressively determined based on the proposed hybrid message. In Algorithm 1, after decryption with private keys,  $\hat{\mathbf{V}}_c$  is extracted from the first  $C$  elements of  $\hat{\mathbf{V}}$  and verified against the  $\bar{\mathbf{V}}_c$  to determine whether the watermark is embedded. If the image is confirmed to be watermarked, the identity message  $\hat{\mathbf{V}}_i$ , derived from the rest elements of  $\hat{\mathbf{V}}$ , is verified against  $\bar{\mathbf{V}}_i$  to access the image authenticity. Bit error rate (BER) is formulated as follows:

$$\text{BER}(\hat{\mathbf{V}}, \bar{\mathbf{V}}) = \frac{\sum_{i=0}^{l-1} \mathbb{1}(\hat{\mathbf{V}}[i] \neq \bar{\mathbf{V}}[i])}{l} \times 100\%, \quad (9)$$

where  $l$  denotes message length.  $\mathbb{1}(\hat{\mathbf{V}}[i] \neq \bar{\mathbf{V}}[i])$  is the indicator function, which equals 1 if  $\hat{\mathbf{V}}[i] \neq \bar{\mathbf{V}}[i]$ , and 0 otherwise. More details of incorporating the RSA algorithm are presented in Appendix A.

## 5 Experiments

### 5.1 Experimental Setup

**Implementation details.** All images are resized to 128 and 256, respectively. The Adam optimizer [Kingma and Ba \(2015\)](#) is used for training 100 epochs with

Table 1: Comparisons of detection performance on CelebA-HQ [Zhu et al \(2022\)](#). The best and secondary results are denoted as **bold** and underline. † denotes the model is tested on  $256 \times 256$ . Since there are two-step determinations, we regard the watermarked image is wrong during the statistics of ACC and F1-Score when  $BER_c^{re} > t_1$ . ‘Pas.’ and ‘Pro.’ denote passive and proactive detectors. ‘SV.’ means self-verification.

Method	Type	SV.	FaceSwap		MobileFS		FaceShifter		SimSwap		MegaFS		E4S		DiffSwap		DiffFace		Avg.↑	
			F1	ACC	F1	ACC	F1	ACC	F1	ACC	F1	ACC	F1	ACC	F1	ACC	F1	ACC	F1	ACC
XceptionRossler et al (2019)	Pas.	-	75.56	71.89	71.30	67.91	57.07	56.77	58.43	59.56	80.06	76.70	66.88	61.19	74.83	71.06	64.89	62.60	68.63	66.38
F3Net Qian et al (2020)	Pas.	-	81.03	<u>91.91</u>	67.64	71.96	57.11	66.33	62.59	65.60	54.68	56.16	80.17	81.02	64.33	69.85	51.36	54.23	64.86	68.38
RECCE Cao et al (2022)	Pas.	-	74.69	66.21	74.70	66.43	74.83	66.40	61.16	67.39	74.87	66.43	74.63	66.18	74.86	66.42	71.05	62.50	72.62	65.99
SBI Shiohara and Yamasaki (2022)	Pas.	-	58.44	62.08	82.66	82.18	67.67	62.90	60.98	62.01	71.13	65.98	69.26	64.30	77.63	72.24	67.34	62.62	69.39	66.79
CADDM Dong et al (2023)	Pas.	-	84.56	82.44	84.23	82.01	80.31	78.27	70.57	69.96	80.45	78.40	80.27	78.23	<u>84.40</u>	<u>82.18</u>	80.56	78.50	80.67	78.75
FPG Xia et al (2024)	Pas.	-	70.66	71.11	83.62	81.93	73.37	73.00	71.81	71.77	82.75	81.11	79.28	77.97	77.52	71.71	77.70	76.59	77.09	75.65
ProDet Cheng et al (2024)	Pas.	-	69.28	64.69	67.29	60.83	74.48	68.89	68.33	62.18	74.64	68.05	70.21	64.42	68.60	66.08	68.42	65.91	70.16	65.16
ODDN Tao et al (2025)	Pas.	-	74.95	69.97	70.86	62.94	73.22	67.37	73.75	69.51	68.81	60.84	68.19	61.56	68.66	62.52	68.53	62.24	70.87	64.62
SepMark† Wu et al (2023b)	Pro.	✓	70.02	57.18	66.89	50.50	71.32	59.80	<b>100</b>	<b>100</b>	70.29	57.74	70.08	57.31	72.33	61.84	77.91	71.64	74.86	64.50
IDMark† Zhao et al (2023b)	Pro.	×	86.77	84.76	<b>97.56</b>	<b>97.32</b>	<u>94.78</u>	<u>94.05</u>	91.06	90.68	<u>96.12</u>	<u>95.96</u>	<b>97.43</b>	<b>97.45</b>	71.57	62.75	93.19	91.82	91.06	89.35
CMark (Ours)	Pro.	✓	<u>91.08</u>	90.37	92.99	92.58	90.66	89.86	92.44	91.96	92.59	92.13	93.18	92.80	83.44	81.28	<u>92.61</u>	<u>92.15</u>	<u>91.12</u>	<u>90.39</u>
CMark† (Ours)	Pro.	✓	<b>94.27</b>	<b>93.96</b>	<u>97.01</u>	<u>96.94</u>	<b>96.62</b>	<b>96.52</b>	<u>95.54</u>	<u>95.37</u>	<b>96.57</b>	<b>96.46</b>	<u>96.35</u>	<u>96.24</u>	<b>85.85</b>	<b>83.62</b>	<b>93.95</b>	<b>93.60</b>	<b>94.52</b>	<b>94.09</b>

$\beta_1=0.5$  and  $\beta_2=0.999$ . The learning rate is set to  $2e^{-4}$  with the batch size equal to 96. We assign  $C=16$  for contour texture and face identity features. There is thus a 32-bit preset message with  $\alpha=0.1$  for each image.  $\lambda_1$  and  $\lambda_2$  are set as 0.1 and 30. During verification,  $t_1$  and  $t_2$  are both set as  $\frac{3}{16} \times 100\%$  as default. The iteration of the morphological dilation is randomly selected within [2, 4] during training. Considering the complex real-world scenarios, we introduce Gaussian Noise, JPEG, Gaussian Blur, Edge Crop, SaltPepper Noise, Median Blur, Resize, Dropout, Brightness, Contrast, Hue, and Saturation distortions during training. All experiments are conducted on four RTX 3090 GPUs.

**Dataset.** The experiments are mainly conducted on CelebA-HQ [Zhu et al \(2022\)](#) for training and testing. To demonstrate the transferability of our approach, we further perform a cross-dataset evaluation on the FFHQ dataset [Karras et al \(2019\)](#).

**Evaluation metrics.** There are two types of BER. One is the comparison between the decoded message and preset message (*i.e.*,  $BER(\hat{\mathbf{V}}, \mathbf{V}^r)$ ). The other is the comparison between the decoded message and reference message (*i.e.*,  $BER(\hat{\mathbf{V}}, \bar{\mathbf{V}})$ ). We briefly denote them as  $BER^{pr}$  and  $BER^{re}$ . Face swapping detection involves accuracy, F1-Score, and  $BER^{re}$ , while watermark robustness is evaluated using  $BER^{pr}$ . We apply PSNR, SSIM, and LPIPS [Zhang et al \(2018\)](#) to assess the quality of the watermarked images. CMark is compared with benchmarks that release code for fairness.

## 5.2 Effectiveness Evaluation

**Face swapping detection.** A comprehensive evaluation in comparison with state-of-the-art passive and proactive detectors is shown in Tab. 1. After embedding

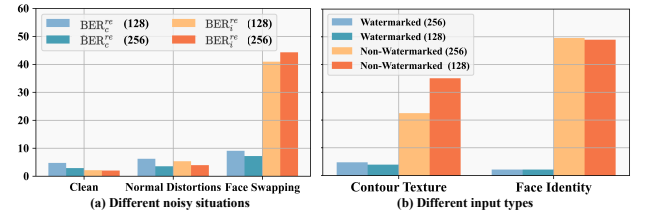


Fig. 6: (a). Average  $BER_c^{re}$  and  $BER_i^{re}$  on different normal image distortions and face swapping techniques. ‘Clean’ means no image distortions. (b).  $BER^{re}$  on watermarked and non-watermarked images.

only 32-bit messages into the images, the average accuracy and F1-Score across 8 face swapping techniques exceed the second-best passive detector over 11.64% and 10.45%, respectively. More importantly, the generalization of our approach is better than other proactive detectors, and this is further demonstrated at  $256 \times 256$  as the embedding space is expanded. Since SepMark [Wu et al \(2023b\)](#) is trained with SimSwap [Chen et al \(2020\)](#), it attains excellent performance in this technique but loses generalization. Although IDMark [Zhao et al \(2023b\)](#) demonstrates comparable performance, its detection performance to DiffSwap [Zhao et al \(2023a\)](#) is severely degraded. The lacking of self-verification also leads to massive storage of preset messages. Additionally, it exhibits a poor visual quality for watermarked images (see Tab. 4). These findings underscore the effectiveness of CMark which simultaneously achieves generalized detection and invisible watermark generation. Fig. 6(a) illustrates the  $BER^{re}$  under different situations.  $BER^{re}$  consists of the face identity error rate  $BER_i^{re}$  and the contour texture error rate  $BER_c^{re}$ . Apparently, the low  $BER_c^{re}$  across different situations indicates the similarity of contour texture between real and swapped images. After face swapping, due to the biases



Table 2: Comparisons of  $BER^{pr}$  under different face swapping techniques. ‘CQ’ and ‘FQ’ indicate CelebA-HQ Zhu et al (2022) and FFHQ Karras et al (2019) datasets. † and ‡ denote the model is evaluated on  $256 \times 256$  and  $512 \times 512$ . The best and secondary results are denoted as **bold** and underline.

Method	FaceSwap		MobileFS		FaceShifter		SimSwap		MegaFS		E4S		DiffSwap		DiffFace		Avg.↓	
	CQ	FQ	CQ	FQ	CQ	FQ	CQ	FQ	CQ	FQ	CQ	FQ	CQ	FQ	CQ	FQ	CQ	FQ
HIDDEN Zhu et al (2018)	16.87	18.89	12.48	12.08	16.24	15.31	27.89	29.49	11.59	11.97	11.49	11.69	24.78	26.53	11.79	11.38	16.64	17.17
PIMOG Fang et al (2022)	8.45	11.28	0.40	<u>0.31</u>	1.23	<b>1.01</b>	8.68	<b>2.99</b>	15.55	17.33	13.07	15.37	17.83	8.25	19.68	18.71	10.61	9.41
ARWGAN Huang et al (2023b)	2.41	4.65	1.70	0.87	2.61	1.49	23.67	25.56	0.96	0.92	<u>1.06</u>	0.96	32.20	18.02	1.16	<b>0.04</b>	8.22	6.56
SepMark Wu et al (2023b)	<b>0.43</b>	<u>2.87</u>	<b>0.05</b>	<b>0.04</b>	<b>0.53</b>	<u>1.37</u>	<u>4.89</u>	5.97	<u>0.36</u>	<u>0.84</u>	0.11	<u>0.37</u>	<b>0.10</b>	<u>0.66</u>	<b>0.17</b>	<u>0.84</u>	<u>0.83</u>	<u>1.62</u>
CMark (Ours)	<u>1.24</u>	<b>0.32</b>	<u>0.21</u>	0.51	<u>0.85</u>	2.83	<b>2.60</b>	<u>5.11</u>	<b>0.29</b>	<b>0.75</b>	<b>0.11</b>	<b>0.34</b>	<u>0.14</u>	<b>0.45</b>	<u>0.23</u>	2.27	<b>0.71</b>	<b>1.57</b>
MBRS† Jia et al (2021)	13.10	14.62	<b>0.98</b>	<b>0.94</b>	1.23	0.69	46.73	47.26	13.96	15.01	13.97	14.96	41.41	9.11	12.36	12.78	17.96	14.42
FaceSigns† Neekhara et al (2022)	50.16	50.09	50.47	49.97	48.91	49.92	50.24	49.78	49.50	49.01	50.27	49.41	46.93	45.51	45.37	44.45	48.98	48.51
SepMark† Wu et al (2023b)	<u>8.70</u>	<u>2.15</u>	11.21	7.69	<b>0.29</b>	<b>0.62</b>	<b>7.91</b>	<b>7.69</b>	4.64	5.32	4.79	5.59	<u>17.33</u>	18.36	<b>0.36</b>	<u>2.61</u>	<u>6.90</u>	<u>6.25</u>
EditGuard‡ Zhang et al (2024a)	84.55	87.27	70.32	71.70	74.54	74.41	48.85	49.59	<u>2.75</u>	<b>2.26</b>	<b>0.21</b>	<b>0.26</b>	75.87	77.89	59.46	60.93	52.06	53.03
CMark† (Ours)	<b>1.42</b>	<b>0.59</b>	<u>2.29</u>	<u>3.01</u>	1.71	3.14	<u>10.16</u>	<u>13.53</u>	<b>1.66</b>	<u>2.45</u>	<u>2.03</u>	<u>2.94</u>	<b>1.54</b>	<b>1.63</b>	<u>0.65</u>	<b>1.42</b>	<b>2.68</b>	<b>3.58</b>

Table 3: Comparisons of  $BER^{pr}$  under normal distortions on CelebA-HQ Zhu et al (2022). † and ‡ denote the model is evaluated on  $256 \times 256$  and  $512 \times 512$ .

Method	GNoise	GBlur	ECrop	JPEG	Avg. ↓
HIDDEN Zhu et al (2018)	48.64	26.96	12.21	32.16	29.99
PIMOG Fang et al (2022)	12.73	0.12	1.74	19.56	8.53
ARWGAN Huang et al (2023b)	46.55	14.78	2.37	42.58	26.57
SepMark Wu et al (2023b)	<u>0.82</u>	<b>0.01</b>	<b>0.01</b>	<b>0.24</b>	<u>0.27</u>
CMark (Ours)	<b>0.47</b>	<u>0.03</u>	<u>0.03</u>	<u>0.46</u>	<b>0.25</b>
MBRS† Jia et al (2021)	41.68	27.95	19.33	0.31	22.32
FaceSigns† Neekhara et al (2022)	0.86	0.17	<u>0.27</u>	0.85	<u>0.54</u>
SepMark† Wu et al (2023b)	<b>0.06</b>	<b>0.01</b>	18.13	<b>0.01</b>	4.55
EditGuard‡ Zhang et al (2024a)	15.81	98.31	3.94	23.62	35.42
CMark† (Ours)	<u>0.31</u>	<u>0.12</u>	<b>0.12</b>	<u>0.73</u>	<b>0.32</b>

in different techniques, the synthesized backgrounds may deviate from the originals and slightly fluctuate the  $BER_c^{re}$ . In contrast, there is a proliferation in  $BER_i^{re}$ , enabling us to set a straightforward threshold for detection rather than building complex classification heads trained in different face swapping techniques.

**Watermark robustness.** Considering the watermark robustness is necessary to ensure accurate face swapping detection, the results on different datasets are summarized in Tab. 2. Apparently, our approach achieves the lowest average  $BER^{pr}$  than other methods, confirming the robustness across various unknown face swapping techniques. Robustness evaluation also involves four representative image distortions that are presented in the first row of Fig. 7. While some methods can achieve better PSNR, the results in Tab. 3 indicate that they are ineffective against normal distortions, which hinders the practicality. The CMark model attains the lowest average  $BER^{pr}$ , demonstrating superior robustness across normal distortions. These results underscore a satisfactory trade-off between visual quality and watermark robustness. The  $BER^{pr}$  results under the more diverse normal distortions are listed in Appendix B.

Table 4: Comparisons of visual quality on CelebA-HQ Zhu et al (2022).

Method	Resolution	Length	PSNR↑	LPIPS↓	SSIM↑
HIDDEN Zhu et al (2018)	128×128	30 bit	33.44	0.0120	0.900
PIMOG Fang et al (2022)	128×128	30 bit	37.73	0.0086	0.947
SepMark Wu et al (2023b)	128×128	30 bit	38.51	<b>0.0028</b>	0.959
ARWGAN Huang et al (2023b)	128×128	30 bit	<b>40.23</b>	0.0063	<u>0.969</u>
EditGuard Zhang et al (2024a)	128×128	30 bit	36.93	-	0.944
CMark (Ours)	128×128	32 bit	<u>39.36</u>	<u>0.0062</u>	<b>0.972</b>
MBRS Jia et al (2021)	256×256	256 bit	<b>44.03</b>	<b>0.0045</b>	<u>0.972</u>
FaceSigns Neekhara et al (2022)	256×256	128 bit	32.33	0.0318	0.921
IDMark Zhao et al (2023b)	256×256	512 bit	28.26	0.0692	0.741
SepMark Wu et al (2023b)	256×256	128 bit	38.56	0.0080	0.933
CMark (Ours)	256×256	32 bit	<u>41.86</u>	<u>0.0068</u>	<b>0.983</b>

**Visual quality.** As illustrated in the last two rows of Fig. 7, the encoded images exhibit imperceptible discrepancies, making them indistinguishable from the human eyes. Leveraging Eq. 4 further decreases the visual differences. Tab. 4 reports the watermarked images generated from the CMark model achieves superior SSIM along with competitive PSNR and LPIPS. The degraded quality is attributed to the limited embedding location, which restricts the integration of the preset messages. Nevertheless, the watermarked images are lossless within the facial regions, effectively preserving the identity of the corresponding original images for downstream face analysis Li et al (2022); Xu et al (2025). More qualitative results of the watermarked images on different datasets are illustrated in Appendix C.

### 5.3 Evaluation under Various Scenarios

**Non-watermarked images.** With the first term specified in Eq. 5, the decoder outputs for non-watermarked images are regularized to 0 and deviate from the magnitude of each element in the preset messages, which promotes distinguishing the non-watermarked images.

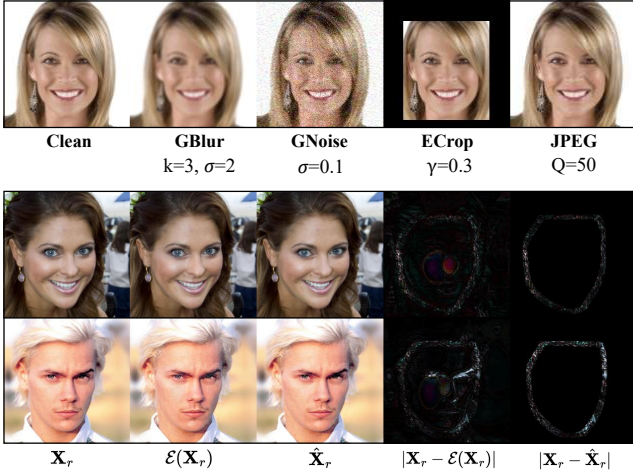


Fig. 7: The **first row** represents the watermarked image under normal distortions. The **last two rows** are the visual comparisons among the original real, encoded, and watermarked images. ‘GNoise’, ‘GBlur’, and ‘ECrop’ denote Gaussian noise, Gaussian blur, and edge crop.  $k$ ,  $\sigma$ ,  $\gamma$ , and  $Q$  denote the kernel size, standard deviation, cropped ratio, and compression quality.

Table 5: Evaluation of cross-dataset performance with different image resolutions on FFHQ Karras et al (2019) dataset.

Metric	Manipulations	FFHQ Karras et al (2019)	
		128×128	256×256
BER <sup>rr</sup> ↓	GNoise	0.46	0.47
	GBlur	0.06	0.17
	ECrop	0.09	0.19
	JPEG	0.60	0.82
	<b>Avg.</b>	0.30	0.41
ACC↑	FaceSwap	90.89	93.46
	MobileFS	91.58	96.58
	FaceShifter	90.29	95.92
	SimSwap	91.33	95.43
	MegaFS	92.94	96.32
	E4S	93.37	97.14
	DiffSwap	80.34	82.76
	DiffFace	90.96	93.50
	<b>Avg.</b>	90.21	93.89

Fig. 6(b) shows the discrepancies of BER<sup>re</sup> when inputting the decoder with the watermarked and non-watermarked images. Noticeably, non-watermarked images yield higher BER<sup>re</sup> than watermarked ones.

**Cross-Dataset evaluation.** Besides the Tab. 2, to assess the transferability of our approach, the CMark model is further evaluated on the FFHQ Karras et al (2019) dataset with different normal distortions and face swapping techniques. Given that contour texture and face identity information are derived from generalized models Zhang et al (2018); Deng et al (2019), the extracted squeezed features exhibit slight deviations.

Table 6: Comparison of visual quality under different resolutions on CelebA-HQ Zhu et al (2022) and FFHQ Karras et al (2019) datasets. ‘IS’ denotes identity similarity compared with the corresponding original images.

Resolution	CelebA-HQ Zhu et al (2022)				FFHQ Karras et al (2019)			
	PSNR ↑	LPIPS ↓	SSIM ↑	IS ↑	PSNR ↑	LPIPS ↓	SSIM ↑	IS ↑
128×128	39.36	0.0062	0.972	0.993	37.53	0.0048	0.962	0.986
256×256	41.86	0.0068	0.983	0.996	41.19	0.0074	0.977	0.991

Table 7: Evaluation of detection robustness on CelebA-HQ dataset Zhu et al (2022).

Swapping Techniques	None	Normal Distortions (ACC ↑)				
		GNoise	GBlur	ECrop	JPEG	<b>Avg.</b>
FaceSwap	90.37	90.21	88.23	88.58	88.78	88.95
MobileFS	92.58	92.09	90.53	91.52	90.69	91.21
FaceShifter	89.86	88.49	81.52	87.68	82.38	85.02
SimSwap	91.96	85.02	87.48	85.80	87.51	86.45
MegaFS	92.13	92.09	90.62	91.76	90.22	91.17
E4S	92.80	92.32	91.34	91.79	91.25	91.68
DiffSwap	81.28	81.04	80.85	80.59	80.16	80.66
DiffFace	92.15	91.45	90.89	90.38	90.80	90.88

Furthermore, the watermark encoding and decoding processes are confined to the contour region within the image, thereby reducing the impact of variation across different datasets. Consequently, the results from Tab. 5 demonstrate similar performance to those observed on the CelebA-HQ Zhu et al (2022) dataset at the 128 and 256 resolutions, respectively. As for visual quality, it can be seen from Tab. 6 that the quantitative results are similar to those of these two datasets, which demonstrates the transferability of our approach. Due to the embedding strategy in the CMark model, there are high identity similarities across different datasets, ensuring the consistency of face analysis between the watermarked images and the corresponding originals. The qualitative results on FFHQ Karras et al (2019) are presented in Fig. 11 of Appendix C.

**Distortions after swapping.** As stated in the threatening Case 2, attackers attempt to interfere with face swapping detectors by introducing additional distortions to the swapped images. We simulate this scenario by applying multiple face swapping techniques and subsequently introduce normal distortions to these images. According to the results in Tab. 7, our approach still maintains superior detection accuracy, which significantly demonstrates the robustness of our approach even if the swapped images are further distorted. Moreover, we further compare the CMark model with the rest of watermark works. As shown in Tab. 8, under SimSwap Chen et al (2020) technique, our approach

Table 8: Comparisons of  $BER^{pr}$  under SimSwap [Chen et al \(2020\)](#) with different image normal distortions on CelebA-HQ [Zhu et al \(2022\)](#).  $\dagger$  and  $\ddagger$  denote the model is tested on  $256 \times 256$  and  $512 \times 512$ .

Method	SimSwap ( $BER^{pr} \downarrow$ )				
	GNoise	GBlur	ECrop	JPEG	Avg.
HIDDEN <a href="#">Zhu et al (2018)</a>	28.76	47.47	39.08	46.89	40.55
PIMOG <a href="#">Fang et al (2022)</a>	21.88	46.56	32.96	47.92	37.33
ARWGAN <a href="#">Huang et al (2023b)</a>	<b>2.34</b>	24.30	<u>6.64</u>	29.36	15.66
SepMark <a href="#">Wu et al (2023b)</a>	2.76	<u>14.83</u>	21.82	<b>4.13</b>	10.89
CMark (Ours)	<u>2.48</u>	<b>9.77</b>	<b>4.49</b>	<u>7.54</u>	<b>6.07</b>
MBRS $^\dagger$ <a href="#">Jia et al (2021)</a>	49.38	45.71	49.12	49.05	48.31
FaceSigns $^\dagger$ <a href="#">Neekhara et al (2022)</a>	49.76	50.01	49.98	49.83	49.89
SepMark $^\dagger$ <a href="#">Wu et al (2023b)</a>	<u>32.26</u>	<u>25.32</u>	<u>20.71</u>	<u>25.57</u>	<u>25.96</u>
EditGuard $^\ddagger$ <a href="#">Zhang et al (2024a)</a>	52.92	49.15	48.91	50.75	50.43
CMark $^\ddagger$ (Ours)	<b>0.31</b>	<b>0.12</b>	<b>0.12</b>	<b>0.73</b>	<b>0.32</b>

Table 9: Ablation under different watermark embedding locations.

Location	SimSwap		ECrop		ECrop+SimSwap	
	$BER^{pr} \downarrow$	ACC $\uparrow$	$BER^{pr} \downarrow$	$BER^{re} \downarrow$	$BER^{pr} \downarrow$	ACC $\uparrow$
All	5.32	82.73	1.13	12.53	22.30	68.79
Background	<b>0.43</b>	<b>93.01</b>	<u>2.21</u>	<u>13.67</u>	<u>19.19</u>	<u>74.83</u>
Contour	<u>2.60</u>	<u>91.96</u>	<b>0.03</b>	<b>10.08</b>	<b>5.99</b>	<b>85.62</b>

maintains the lowest  $BER^{pr}$  across various distortions, validating the strong robustness of our approach.

#### 5.4 Ablation Study

**Embedding location.** To ensure the detection generalization, the CMark model is trained without any swapping techniques. The embedding location is thus important to ensure the watermark robustness. Tab. 9 shows different embedding configurations. When encountering the swapping technique, the robustness is degraded after embedding into entire images as the facial regions are severely tampered. While embedding the background mitigates this impact, the robustness can not be maintained after attackers further crop the background (see threatening Case 1). Since the contour belongs to the subpart of the background and closely attaches to the face, it can be simultaneously less susceptible to malicious cropping and face swapping.

**Detection threshold.** Given the threshold overfitting when excessively adjusting  $t_1$  and  $t_2$  to adapt specific manipulations, we briefly let  $t_1=t_2$  during the optimal threshold searching. As shown in Tab. 10, a lower threshold reduces detection performance as a large number of watermarked real images are predicted as either non-watermarked or watermarked fake images. Conversely, a higher threshold leads to misclassifying watermarked fake images as real ones.

Table 10: Ablation of threshold under SimSwap [Chen et al \(2020\)](#) on CelebA-HQ [Zhu et al \(2022\)](#) dataset.

Threshold	128 $\times$ 128		256 $\times$ 256	
	ACC $\uparrow$	F1-Score $\uparrow$	ACC $\uparrow$	F1-Score $\uparrow$
1/16	59.66	63.83	69.17	73.41
2/16	81.08	83.28	88.12	88.85
3/16	<b>91.96</b>	<b>92.44</b>	<b>95.54</b>	<b>95.37</b>
4/16	<u>90.88</u>	<u>91.27</u>	<u>93.36</u>	<u>93.66</u>
5/16	86.23	88.03	90.37	91.13

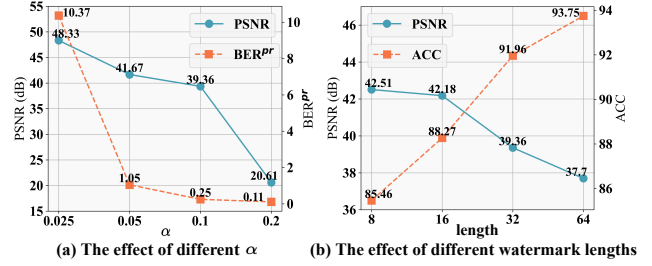


Fig. 8: Ablation study of  $\alpha$  and watermark length to the CMark model. (a)  $BER^{pr}$  is computed by average the results from the GNoise, GBlur, ECrop, and JPEG distortions. (b) Detection accuracy is calculated based on the swapped images from SimSwap.

**Strength factor.** Fig. 8(a) shows the effect of varying strength factor  $\alpha$ . Apparently, a smaller  $\alpha$  enhances watermark imperceptibility but dramatically compromises robustness against normal distortions. Conversely, a larger  $\alpha$  results in a significant degradation of visual quality. An optimal balance between imperceptibility and robustness is achieved when  $\alpha=0.1$ .

**Watermark length.** Fig. 8(b) depicts the influence of watermark length. It can be seen that a watermark length of 32 strikes an effective trade-off between imperceptibility and detection accuracy. A shorter length leads to low detection accuracy as the  $BER_{out}$  of the real and swapped face images become less distinguishable and prone to misjudgment. On the other hand, a longer watermark length degrades visual quality due to the increased embedded information.

**Components effectiveness.** To verify the effectiveness of each component, we examine the proactive denoiser (PD), the utilization of watermarked images (WI), and the contour mask constraint (MC). Results are listed in Tab. 11. (a) PD: Contour mask consistency is important to ensure the decoding correctness. Furthermore, the extracted reference messages are significantly impacted by the normal distortions. Without the denoiser, the  $BER^{re}$  thus increases following distortion of the watermarked images. After employing the denoiser, normal distorted images are standardized to a pattern closer to the clean, thereby reducing  $BER^{re}$ . (b) WI: There is no difference in  $BER^{pr}$  when utilizing

Table 11: Ablation under different configurations in CMark model.

Case	MC	WIPD	Distortions	BER <sup>pr</sup> ↓	BER <sup>re</sup> ↓	PSNR ↑	SSIM ↑
(a)	✓	✓	-	0.02	<b>2.94</b>	39.36	0.971
(a)	✓	✓	✓	0.27	6.82	39.36	0.971
(b)	✓	-	✓	0.02	4.69	37.02	0.946
(c)	-	✓	✓	<u>0.05</u>	3.98	39.42	0.977
(c)	-	✓	✓	0.89	7.38	<b>39.42</b>	<b>0.977</b>
Ours	✓	✓	✓	<b>0.02</b>	<u>3.45</u>	<u>39.36</u>	<u>0.972</u>
	✓	✓	✓	0.25	5.79	39.36	0.972

the encoded images as the inputs of watermark decoder. However, due to reconstruction biases in  $\mathcal{E}$ , the visual quality declines without fusing the original images by Eq. 4. (c) MC: Without the constraint in each block during training, watermark features integrate the entire image features, enhancing invisibility but leading to higher error rates after distortions.

## 6 Limitations and Future Perspective

While the CMark model demonstrates promising performance in detecting face swapped images, its generalization to other face forgery types, such as face reenactment and editing, requires further investigation. Moreover, future work will also aim to enhance the model robustness against adversarial attacks, particularly in untrusted client-side deployment scenarios.

## 7 Conclusion

To generalize the defense against different unknown face swapping techniques, we start from the face swapping purpose and propose a proactive detector that requires neither face swapping techniques for training nor large-scale message storage. CMark model focuses on the contour region surrounding the face and embeds the contour texture and face identity information into the images. Asymmetric encryption secures the model during message communication. Extensive experiments validate the generalization of face swapping detection, the visual quality of watermarked images, and the robustness of watermark across multiple scenarios.

## Appendix A Explanation of Encryption and Decryption

Given a  $\phi = (p-1) \cdot (q-1)$ , where  $p$  and  $q$  are different prime numbers. A public key  $e$  is randomly generated as follows:

$$\text{GCD}(\phi, e) = 1, \text{ s.t. } e \in (1, \phi), \quad (10)$$

where  $\text{GCD}(\cdot)$  indicates the function of greatest common divisor. The private key  $d$  is computed by:

$$d \cdot e \equiv 1 \pmod{\phi}, \quad (11)$$

where  $d$  mathematically represents the modular multiplicative inverse of  $e$  modulo  $\phi$ . Therefore, the encryption function  $\text{RSA\_En}(\cdot)$  *w.r.t.* message  $\mathbf{V}$  is expressed:

$$\mathbf{E}_v \equiv \text{Bin}(\text{Int}(\mathbf{V})^e \pmod{p \cdot q}), \quad (12)$$

where  $\text{Int}(\cdot)$  denotes the conversion of a binary number to its decimal equivalent, and  $\text{Bin}(\cdot)$  refers to the conversion of a decimal number to its binary representation. During the decryption,  $\text{RSA\_De}(\cdot)$  *w.r.t.*  $\mathbf{E}_v$  is formulated as follows:

$$\mathbf{V} \equiv \text{Bin}(\text{Int}(\mathbf{E}_v)^d \pmod{p \cdot q}). \quad (13)$$

When the product  $p \cdot q$  is sufficiently large, reversing the  $p$  and  $q$  becomes computationally infeasible. This increases the difficulty of deciphering  $\phi$ , thereby ensuring the security of  $d$ , even if attackers know the  $e$  and Eq.(11). Consequently,  $\mathbf{V}$  can be effectively prevented from interception.

## Appendix B Robustness under More Image Distortions

To validate the robustness of the CMark, we introduce more image normal distortions and compare it with other methods. The BER<sup>pr</sup> under these normal distortions are listed in Tab. 12. Apparently, our approach surpasses the secondary method Wu et al (2023b) by over 1.24% on average at 256×256 and attains comparable results at 128×128 resolution, respectively. After simulating the reconstruction distortion through the proposed denoiser, the robustness is severely degraded for FaceSigns Neekhara et al (2022). However, the robustness of CMark is still maintained with few fluctuations, validating the robustness of our approach in challenging scenarios. Additional distorted watermarked instances are presented in Fig. 9.

## Appendix C More Illustrations of Watermarked Images

Fig. 10 illustrates more watermarked images on CelebA-HQ Zhu et al (2022). While the discrepancies between the encoded and original images are primarily located in the face contour, extra discrepancies can also be observed in the background or internal facial



Table 12: Comparisons of  $BER^{pr}$  on CelebA-HQ. The best and secondary are denoted as **bold** and underline. ‘GNoise’, ‘GBlur’, ‘ECrop’, ‘MBlur’, and ‘Rec.’ mean GaussianNoise, GaussianBlur, EdgeCrop, MedianBlur, and reconstruction. † and ‡ mean the model is tested on  $256 \times 256$  and  $512 \times 512$ , respectively.

Method	GNoise	GBlur	ECrop	JPEG	SaltPepper	MBlur	Resize	Dropout	Brightness	Contrast	Hue	Saturation	Rec.	Avg. ↓
HIDDEN <a href="#">Zhu et al (2018)</a>	48.64	26.96	12.21	32.16	23.13	17.53	18.29	13.21	11.28	11.38	13.79	11.16	19.21	19.91
PIMOG <a href="#">Fang et al (2022)</a>	12.73	0.12	1.74	19.56	2.58	0.07	0.05	0.64	1.21	0.68	0.14	0.07	0.13	3.05
ARWGAN <a href="#">Huang et al (2023b)</a>	46.55	14.78	2.37	42.58	21.13	1.14	7.51	5.15	1.02	0.91	2.94	0.86	9.08	12.00
SepMark <a href="#">Wu et al (2023b)</a>	0.82	0.01	0.01	0.24	0.03	0.01	0.01	0.01	0.01	0.01	0.01	0.01	0.01	<b>0.09</b>
CMark	0.47	0.03	0.03	0.46	0.08	0.04	0.13	0.02	0.02	0.06	0.03	0.02	0.30	<u>0.13</u>
MBRS <sup>†</sup> <a href="#">Jia et al (2021)</a>	41.68	27.95	19.33	0.31	30.85	2.56	2.26	7.99	0.92	1.13	0.01	0.01	0.02	10.38
FaceSigns <sup>†</sup> <a href="#">Neehara et al (2022)</a>	0.86	0.17	0.27	0.85	12.75	0.11	1.02	1.85	8.41	0.02	0.76	0.05	13.54	3.12
SepMark <sup>†</sup> <a href="#">Wu et al (2023b)</a>	0.06	0.01	18.13	0.01	0.01	0.01	0.01	0.01	0.01	0.01	0.01	0.01	0.01	<u>1.41</u>
EditGuard <sup>‡</sup> <a href="#">Zhang et al (2024a)</a>	15.81	98.31	3.94	23.62	3.68	93.59	49.88	0.84	0.32	0.39	4.15	0.55	51.47	26.65
CMark <sup>†</sup>	0.31	0.12	0.12	0.73	0.01	0.12	0.13	0.13	0.19	0.21	0.01	0.11	0.14	<b>0.17</b>

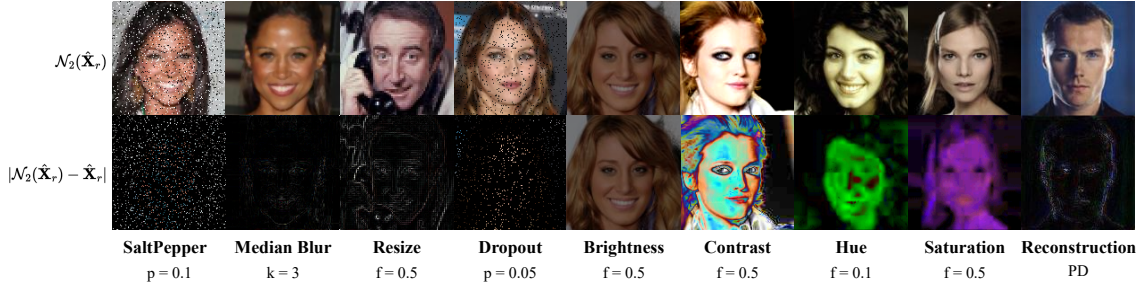


Fig. 9: **Qualitative results of watermarked images under different normal distortions on CelebA-HQ** [Zhu et al \(2022\)](#). Each column in the first row corresponds to one type of distortion. ‘p’ denotes the distorted probability that attaches to each pixel. ‘k’ is the kernel size, ‘f’ represents the deviation factor related to specific distortions, and ‘PD’ means the proposed proactive denoiser. All image sizes are equal to  $128 \times 128$ .

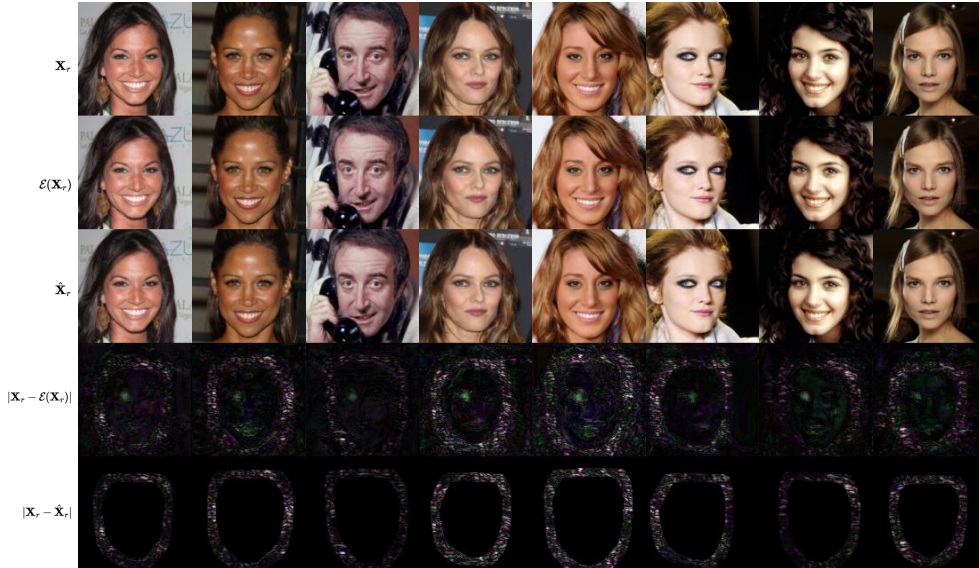


Fig. 10: Qualitative results on CelebA-HQ [Zhu et al \(2022\)](#) dataset. All image sizes are equal to  $128 \times 128$ .

regions. These extra discrepancies in the encoded images arise from the reconstruction biases introduced by the watermark encoder. Accordingly, applying Eq. 4 is important to mitigate these reconstruction biases, thereby improving the visual quality while maintaining the watermark robustness. Furthermore, the qualitative results on FFHQ [Karras et al \(2019\)](#) are presented

in Fig. 11. The visual discrepancies between the original images and the corresponding watermarked images remain indistinguishable to human eyes, ensuring the imperceptibility of the embedded watermark.

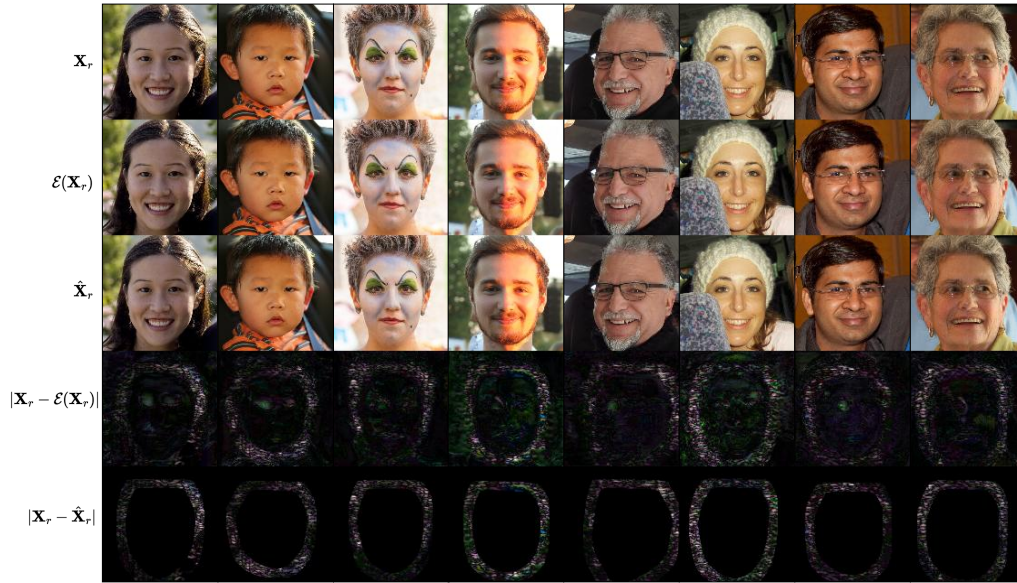


Fig. 11: Qualitative results on FFHQ Karras et al (2019) dataset. All image sizes are equal to  $128 \times 128$ .

## References

- Abdi H, Williams LJ (2010) Principal component analysis. *Wiley interdisciplinary reviews: computational statistics* 2(4):433–459
- Cao J, Ma C, Yao T, Chen S, Ding S, Yang X (2022) End-to-end reconstruction-classification learning for face forgery detection. In: *Proceedings of the IEEE/CVF Conference on Computer Vision and Pattern Recognition (CVPR)*, pp 4113–4122
- Chen R, Chen X, Ni B, Ge Y (2020) Simswap: An efficient framework for high fidelity face swapping. In: *Proceedings of the 28th ACM international conference on multimedia*, pp 2003–2011
- Cheng J, Yan Z, Zhang Y, Luo Y, Wang Z, Li C (2024) Can we leave deepfake data behind in training deepfake detector? *arXiv preprint arXiv:240817052*
- Deng J, Guo J, Xue N, Zafeiriou S (2019) Arcface: Additive angular margin loss for deep face recognition. In: *Proceedings of the IEEE/CVF conference on computer vision and pattern recognition*, pp 4690–4699
- Dong S, Wang J, Ji R, Liang J, Fan H, Ge Z (2023) Implicit identity leakage: The stumbling block to improving deepfake detection generalization. In: *Proceedings of the IEEE/CVF Conference on Computer Vision and Pattern Recognition*, pp 3994–4004
- Fang H, Jia Z, Ma Z, Chang EC, Zhang W (2022) Pimog: An effective screen-shooting noise-layer simulation for deep-learning-based watermarking network. In: *Proceedings of the 30th ACM international conference on multimedia*, pp 2267–2275
- Heusel M, Ramsauer H, Unterthiner T, Nessler B, Hochreiter S (2017) Gans trained by a two time-scale update rule converge to a local nash equilibrium. *Advances in neural information processing systems* 30
- Ho J, Jain A, Abbeel P (2020) Denoising diffusion probabilistic models. *Advances in neural information processing systems* 33:6840–6851
- Hu J, Shen L, Sun G (2018) Squeeze-and-excitation networks. In: *Proceedings of the IEEE conference on computer vision and pattern recognition*, pp 7132–7141
- Huang B, Wang Z, Yang J, Ai J, Zou Q, Wang Q, Ye D (2023a) Implicit identity driven deepfake face swapping detection. In: *Proceedings of the IEEE/CVF conference on computer vision and pattern recognition*, pp 4490–4499
- Huang J, Luo T, Li L, Yang G, Xu H, Chang CC (2023b) Arwgan: Attention-guided robust image watermarking model based on gan. *IEEE Transactions on Instrumentation and Measurement* 72:1–17
- iProov (2024) New threat intelligence report exposes the impact of generative ai on remote identity verification. <https://www.iproov.com/press/new-threat-intelligence-report-exposes-impact-generative-ai-remote-identity-verification>
- Jia Z, Fang H, Zhang W (2021) Mbrs: Enhancing robustness of dnn-based watermarking by mini-batch of real and simulated jpeg compression. In: *Proceedings of the 29th ACM international conference on multimedia*, pp 41–49
- Karras T, Aila T, Laine S, Lehtinen J (2017) Progressive growing of gans for improved quality, stability, and variation. *CoRR* abs/1710.10196, URL <http://arxiv.org/abs/1710.10196>, 1710.10196

- Karras T, Laine S, Aila T (2019) A style-based generator architecture for generative adversarial networks. In: Proceedings of the IEEE/CVF conference on computer vision and pattern recognition, pp 4401–4410
- Kaur D, Uslu S, Rittichier KJ, Durresi A (2022) Trustworthy artificial intelligence: a review. *ACM computing surveys (CSUR)* 55(2):1–38
- Kim K, Kim Y, Cho S, Seo J, Nam J, Lee K, Kim S, Lee K (2022) Diffface: Diffusion-based face swapping with facial guidance. *arXiv preprint arXiv:221213344*
- Kingma DP, Ba J (2015) Adam: A method for stochastic optimization. In: 3rd International Conference on Learning Representations, ICLR
- Li B, Qi P, Liu B, Di S, Liu J, Pei J, Yi J, Zhou B (2023) Trustworthy ai: From principles to practices. *ACM Computing Surveys* 55(9):1–46
- Li H, Wang N, Yang X, Wang X, Gao X (2022) Towards semi-supervised deep facial expression recognition with an adaptive confidence margin. In: Proceedings of the IEEE/CVF conference on computer vision and pattern recognition, pp 4166–4175
- Li L, Bao J, Yang H, Chen D, Wen F (2019) Faceshifter: Towards high fidelity and occlusion aware face swapping. *arXiv preprint arXiv:191213457*
- Li L, Bao J, Zhang T, Yang H, Chen D, Wen F, Guo B (2020) Face x-ray for more general face forgery detection. In: Proceedings of the IEEE/CVF conference on computer vision and pattern recognition, pp 5001–5010
- Liu MH, Cheng H, Wang T, Luo X, Xu XS (2025a) Learning real facial concepts for independent deepfake detection. *arXiv preprint arXiv:250504460*
- Liu MH, Liu XQ, Luo X, Xu XS (2025b) Data: Multi-disentanglement based contrastive learning for open-world semi-supervised deepfake attribution. *arXiv preprint arXiv:250504384*
- Liu Z, Li M, Zhang Y, Wang C, Zhang Q, Wang J, Nie Y (2023) Fine-grained face swapping via regional gan inversion. In: Proceedings of the IEEE/CVF conference on computer vision and pattern recognition, pp 8578–8587
- Mittal A, Soundararajan R, Bovik AC (2012) Making a “completely blind” image quality analyzer. *IEEE Signal processing letters* 20(3):209–212
- Neekhara P, Hussain S, Zhang X, Huang K, McAuley J, Koushanfar F (2022) Facesigns: semi-fragile neural watermarks for media authentication and countering deepfakes. *arXiv preprint arXiv:220401960*
- Nichol AQ, Dhariwal P (2021) Improved denoising diffusion probabilistic models. In: International conference on machine learning, PMLR, pp 8162–8171
- Qian Y, Yin G, Sheng L, Chen Z, Shao J (2020) Thinking in frequency: Face forgery detection by mining frequency-aware clues. In: European conference on computer vision, Springer, pp 86–103
- Rivest R (1978) A method for obtaining digital signatures and public-key cryptosystems. *Communications of the ACM*
- Rombach R, Blattmann A, Lorenz D, Esser P, Ommer B (2021) High-resolution image synthesis with latent diffusion models. [2112.10752](https://arxiv.org/abs/2112.10752)
- Rossler A, Cozzolino D, Verdoliva L, Riess C, Thies J, Nießner M (2019) Faceforensics++: Learning to detect manipulated facial images. In: Proceedings of the IEEE/CVF international conference on computer vision, pp 1–11
- Shiohara K, Yamasaki T (2022) Detecting deepfakes with self-blended images. In: Proceedings of the IEEE/CVF Conference on Computer Vision and Pattern Recognition, pp 18720–18729
- Song J, Meng C, Ermon S (2020) Denoising diffusion implicit models. *arXiv preprint arXiv:201002502*
- Szegedy C, Vanhoucke V, Ioffe S, Shlens J, Wojna Z (2016) Rethinking the inception architecture for computer vision. In: Proceedings of the IEEE conference on computer vision and pattern recognition, pp 2818–2826
- Tao R, Le M, Tan C, Liu H, Qin H, Zhao Y (2025) Oddn: Addressing unpaired data challenges in open-world deepfake detection on online social networks. In: Proceedings of the AAAI Conference on Artificial Intelligence, vol 39, pp 799–807
- Walczyna T, Piotrowski Z (2023) Quick overview of face swap deep fakes. *Applied Sciences* 13(11):6711
- Wang R, Juefei-Xu F, Luo M, Liu Y, Wang L (2021) Faketag: Robust safeguards against deepfake dissemination via provenance tracking. In: Proceedings of the 29th ACM international conference on multimedia, pp 3546–3555
- Wang T, Huang M, Cheng H, Ma B, Wang Y (2023) Robust identity perceptual watermark against deepfake face swapping. *arXiv preprint arXiv:231101357*
- Wang T, Huang M, Cheng H, Zhang X, Shen Z (2024a) Lampmark: Proactive deepfake detection via training-free landmark perceptual watermarks. In: Proceedings of the 32nd ACM International Conference on Multimedia, pp 10515–10524
- Wang T, Liao X, Chow KP, Lin X, Wang Y (2024b) Deepfake detection: A comprehensive survey from the reliability perspective. *ACM Computing Surveys*
- Wu H, Xiang S, Gabriben, Nicezm (2020) Faceswap. <https://github.com/wuhuikai/FaceSwap>
- Wu J, Gan W, Chen Z, Wan S, Lin H (2023a) Ai-generated content (aigc): A survey. *arXiv preprint arXiv:230406632*



- Wu X, Liao X, Ou B (2023b) Sepmark: Deep separable watermarking for unified source tracing and deepfake detection. In: Proceedings of the 31st ACM International Conference on Multimedia
- Xia R, Zhou D, Liu D, Yuan L, Wang S, Li J, Wang N, Gao X (2024) Advancing generalized deepfake detector with forgery perception guidance. In: Proceedings of the 32nd ACM International Conference on Multimedia, pp 6676–6685
- Xu Y, Li H, Zhu M, Wang N, Gao X (2025) Boosting semi-supervised facial attribute recognition with dynamic threshold pairs. *IEEE Transactions on Circuits and Systems for Video Technology*
- Xu Z, Hong Z, Ding C, Zhu Z, Han J, Liu J, Ding E (2022) Mobilefaceswap: A lightweight framework for video face swapping. In: Proceedings of the AAAI Conference on Artificial Intelligence, vol 36, pp 2973–2981
- Yan Z, Zhao Y, Chen S, Guo M, Fu X, Yao T, Ding S, Yuan L (2024) Generalizing deepfake video detection with plug-and-play: Video-level blending and spatiotemporal adapter tuning. *arXiv preprint arXiv:240817065*
- Zhang R, Isola P, Efros AA, Shechtman E, Wang O (2018) The unreasonable effectiveness of deep features as a perceptual metric. In: Proceedings of the IEEE conference on computer vision and pattern recognition, pp 586–595
- Zhang X, Li R, Yu J, Xu Y, Li W, Zhang J (2024a) Editguard: Versatile image watermarking for tamper localization and copyright protection. In: Proceedings of the IEEE/CVF conference on computer vision and pattern recognition, pp 11964–11974
- Zhang Y, Ye D, Xie C, Tang L, Liao X, Liu Z, Chen C, Deng J (2024b) Dual defense: Adversarial, traceable, and invisible robust watermarking against face swapping. *IEEE Transactions on Information Forensics and Security*
- Zhao W, Rao Y, Shi W, Liu Z, Zhou J, Lu J (2023a) Diffswap: High-fidelity and controllable face swapping via 3d-aware masked diffusion. In: Proceedings of the IEEE/CVF Conference on Computer Vision and Pattern Recognition, pp 8568–8577
- Zhao Y, Liu B, Ding M, Liu B, Zhu T, Yu X (2023b) Proactive deepfake defence via identity watermarking. In: Proceedings of the IEEE/CVF winter conference on applications of computer vision, pp 4602–4611
- Zhou J, Li Y, Wu B, Li B, Dong J, et al (2024) Freqlblender: Enhancing deepfake detection by blending frequency knowledge. *Advances in Neural Information Processing Systems* 37:44965–44988
- Zhu H, Wu W, Zhu W, Jiang L, Tang S, Zhang L, Liu Z, Loy CC (2022) Celebv-hq: A large-scale video facial attributes dataset. In: European conference on computer vision, Springer, pp 650–667
- Zhu J, Kaplan R, Johnson J, Fei-Fei L (2018) Hidden: Hiding data with deep networks. In: Proceedings of the European Conference on Computer Vision (ECCV)
- Zhu Y, Li Q, Wang J, Xu CZ, Sun Z (2021) One shot face swapping on megapixels. In: Proceedings of the IEEE/CVF conference on computer vision and pattern recognition, pp 4834–4844